Langtaosha (LTS) Preprint doi: https://doi.org/10.65215/tr794007 This version posted December 4, 2025. The copyright holder for this preprint (which was not certified by peer review) is the author/funder. Creative Commons license: CC Attribution-NonCommercial-NoDerivatives 4.0 https://creativecommons.org/licenses/by-nc-nd/4.0

Performance Evaluation of the SmartBrain: A Wearable PET System for Human Brain Imaging

Han Liu[1,2], Wenkang Qu[1], Da Liang[1], Xin Yu[1], Yuejie Lin[1], Haoyu Zhou[1], Siyuan Han[1], Zhijun Zhao[1], Ying Lin[1], Xiaoyin Zhang[1], Jinyong Tao[1], Wenbin Li[1], Huiping Zhao[1], Yibin Zhang[1], Gongning Luo[2] , Ningyi Jiang[3], Qiyu Peng[1]*

[1]Institute of Biomedical Engineering, Shenzhen Bay Laboratory, Shenzhen, China

[2]College of Artificial Intelligence, Harbin Institute of Technology, Harbin, China

[3]Department of Nuclear Medicine, The Seventh Affiliated Hospital, Sun Yat-sen University, Shenzhen, China

Abstract—Background. Positron Emission Tomography (PET) is a vital medical imaging tool for studying in vivo metabolism. However, conventional PET systems are limited in their inability to image during free movement. Therefore, we have developed a wearable brain PET system for real-time imaging, called SmartBrain. ***Methods.*** The SmartBrain used 192 detectors and the detector consists of a 6 × 6 lutetium-yttrium oxyorthosilicate crystal (3 × 3 × 5 mm^3) array with 3 × 3 silicon photomultipliers array. We evaluated the physical performance of SmartBrain according to the National Electrical Manufacturers Association (NEMA) NU 2-2018 standard. In addition, we performed ^{18}F-FDG imaging using a custom Hoffman brain phantom and a multi-layer Derenzo phantom. Dynamic rat images and the ^{18}F-FDG images from a healthy volunteer are presented. ***Results.*** Spatial resolution is 2.29 mm in center of field of view (FOV). The sensitivity was 720.15 cps/MBq. The peak noise-equivalent count rate was 4.67 kcps at 10.11 kBq/ml, and the scatter fraction was 29.53%. The NEMA image-quality contrast recovery coefficients varied from 72.85% (10-mm sphere) to 89.40% (37-mm sphere), and background variability was 11.25% at a contrast of 9.36:1. The time-of-flight (TOF) resolution was 234.22 ps, and the energy resolution was 10.81%. The SmartBrain showed that the main structures of Hoffman brain phantom could be resolved and demonstrated the ability to separate rods as small as 1.7 mm. In addition, an example of the structure of the human brain was demonstrated. ***Conclusion.*** The SmartBrain clearly demonstrated brain structures, confirming its suitability for clinical brain research. Moreover, as a wearable and mobile PET platform, it offers unique opportunities for naturalistic brain imaging and future clinical applications in the diagnosis and management of neurological disorders.

Keywords— Wearable PET, Human brain imaging, NEMA, SmartBrain

Langtaosha (LTS) Preprint doi: https://doi.org/10.65215/tr794007 This version posted December 4, 2025. The copyright holder for this preprint (which was not certified by peer review) is the author/funder. Creative Commons license: CC Attribution-NonCommercial-NoDerivatives 4.0 https://creativecommons.org/licenses/by-nc-nd/4.0

I. Introduction

Human brain research is essential for understanding cognition, emotion, and behavior. Brain PET is a powerful imaging modality that directly reflects cerebral metabolic activity, making it an essential tool for human brain research (1,2). However, conventional brain PET typically requires subjects to remain stationary in a sitting or supine position during scanning, which poses limitations for certain patient populations, such as children, individuals with epilepsy, or patients with other neurological disorders. Wearable brain PET systems aim to address these challenges by enabling brain metabolism studies in more natural or even dynamic conditions, thereby expanding the potential applications of brain PET in neuroscience and clinical research. Moreover, wearable brain PET systems are highly portable, require less space, and are more cost-effective, which could allow this technology to be extended to a broader user base, benefiting more people.

Despite this potential, research on mobile or wearable brain PET systems remains at an early stage. In 2011, Yamamoto and colleagues from Nagoya University, Japan, developed a seated PET brain imaging system specifically designed for human studies, known as PET-Hat (3). Subsequently, Tashima's team in Japan introduced a similar seated PET system known as Helmet-Chin PET (4). However, both systems require stationary mounting platforms, limiting their use in portable imaging contexts. In 2017, Brefczynski-Lewis's group at West Virginia University developed a semi-mobile brain PET system, known as AM-PET (5), by mounting the PET scanner on an externally movable support. In the same year, Peng's group further advanced this technology by creating the Mind-tracker PET (6), a fully wearable brain PET system weighing only 3.5 kg that operated without an external support structure. However, both AM-PET and Mind-tracker PET had limited axial fields of view (50 mm and 30 mm, respectively), restricting imaging to small regions of the brain. Moreover, these systems lacked TOF measurement capabilities (7).

This work aims to develop a wearable brain PET system capable of imaging in free movement. To verify whether the SmartBrain PET can meet the basic standards of commercial PETs, we have evaluated system performance using the NEMA NU 2-2018 standards and compare it with the GE Discovery MI PET/CT system (GE DMI) to ensure its practicality and effectiveness. And we will validate its potential value in real-world scenarios in future work.

II. Methods

A. System Parameters

The SmartBrain PET system features a 16-sided polygonal ring with an inner diameter of 207.44 mm and an axial field of view (AFOV) of 121 mm, covering the entire brain (Figure 1). It consists of 192 detector modules arranged in six rings, with 32 modules per ring with 0.5 mm axial and tangential gaps. Each module comprises a 6 × 6 array of 3 × 3 × 5 mm^3 lutetium-yttrium

Langtaosha (LTS) Preprint doi: https://doi.org/10.65215/tr794007 This version posted December 4, 2025. The copyright holder for this preprint (which was not certified by peer review) is the author/funder. Creative Commons license: CC Attribution-NonCommercial-NoDerivatives 4.0 https://creativecommons.org/licenses/by-nc-nd/4.0

oxyorthosilicate (LYSO) crystals, optically coupled via optical adhesive to a 3 × 3 array of 6-mm silicon photomultipliers (SiPMs; onsemi, Phoenix, AZ, USA).

A channel reduction strategy decreases the total number of readout channels from 1,728 to 432. Each detector module integrates a 3 × 3 SiPM array. Four modules are combined in a 2 × 2 configuration, and signals are hierarchically multiplexed from 36 channels to 9 by encoding three rows, three columns, and three logical layers, with the fourth layer inferred from the others (8). To further reduce system weight, the 5-mm-thick crystals were used, at the cost of lower sensitivity and signal-to-noise ratio (SNR). Future integration of TOF is expected to improve SNR (9). The use of channel reduction and lightweight crystals results in an overall system weight of approximately 6 kg.

The system supports list-mode acquisition (461–611 keV energy window, 1 ns coincidence window), with a decoding algorithm ensuring accurate event positioning. Data are timestamped for flexible post-processing, supporting TOF and dynamic imaging. Two mechanical support systems were developed: a wearable backpack and a suspension system (Figure 1). Temperature is stabilized within 0.5 ℃ using external fans and air-cooled ducts.

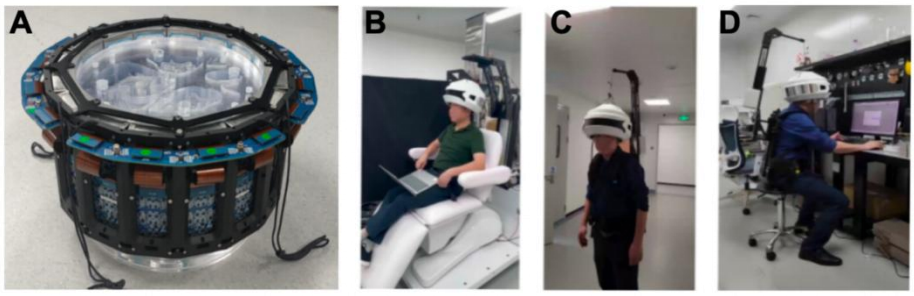

FIGURE 1. The SmartBrain PET system. (A) System composed of detectors and SiPMs with Hoffman phantom. (B) Seated-position scanning. (C) Backpack system permitting data collection in ambulatory states. (D) Workstation scenario demonstrating natural seated use.

B. NEMA NU 2-2018 Performance evaluation

Physical performance was evaluated according to the NEMA NU 2-2018 standards (10), including spatial resolution, sensitivity, count rate performance, accuracy of corrections, image quality, energy and timing resolution.

Spatial Resolution. Spatial resolution was measured at 16 different locations, with 60-second acquisitions at each point (8 points at the center of the axial FOV, 8 points at one-eighth of the axial FOV from the end of the tomography), using a 0.25 mm ^{22}Na point source (0.444 MBq) embedded in a solid disk. The data were reconstructed using a two-dimensional filtered backprojection (FBP2D) algorithm without any correction, with a voxel size of 0.543 × 0.543 × 1.625 mm^3. To meet the NEMA requirement that the voxel size be smaller than one-third of the full width at half maximum (FWHM), the reconstructed images

Langtaosha (LTS) Preprint doi: https://doi.org/10.65215/tr794007 This version posted December 4, 2025. The copyright holder for this preprint (which was not certified by peer review) is the author/funder. Creative Commons license: CC Attribution-NonCommercial-NoDerivatives 4.0 https://creativecommons.org/licenses/by-nc-nd/4.0

were resampled using trilinear interpolation to achieve an isotropic voxel size of 0.5 × 0.5 × 0.5 mm^3. Axial, radial, and tangential resolutions were evaluated according to the NEMA NU 2-2018 standard.

Sensitivity. Sensitivity measurements were performed using a NEMA PET sensitivity phantom consisting of five concentric aluminum sleeves, each 70 cm in length. A 70-cm polyethylene tube filled with 5.1 MBq of ^{18}F-FDG solution was inserted into the aluminum sleeves, positioned both at the center of the transaxial FOV and 5 cm off-center. Ten 600-second acquisitions were conducted, successively removing the outermost sleeve to estimate attenuation-free sensitivity. The collected list-mode data were binned into sinograms using single-slice rebinning to estimate both total sensitivity and axial slice sensitivity.

Count Rate Performance. Count rate performance was evaluated using a scatter phantom consisting of a 14 cm long polyethylene cylinder with a 10 cm diameter. The line source was initially loaded with 41.86 MBq of ^{18}F-FDG at the first measurement start and 1.17 MBq at the last measurement start. In total, we scanned 34 frames with 60 s durations as the activity decayed. System count rates were plotted alongside activity concentrations, including trues, randoms, scatters, total counts, the noise-equivalent count rate and scatter fraction without any correction.

Image Quality. We developed a brain-sized image quality phantom to replace the human torso, which had six spheres as the original phantom. A cylindrical phantom with a liquid-filled diameter of 19 cm was filled with ^{18}F-FDG at a background activity concentration of 4.06 kBq/ml. Six spheres with diameters of 10, 13, 17, 22, 28 and 37 mm were filled with the ^{18}F-FDG solution at an activity concentration with a sphere-to-background ratio of 9.36:1. Measurement duration was 60 min. Contrast of hot spheres (QH) and background variability (Nj) were measured. To evaluate background variability, twelve circular ROIs were placed on the background uniform region over 5 axial slices (60 ROIs in total), with the same diameter as hot sphere. Images were reconstructed using the ordered-subset expectation maximization (OSEM) algorithm for 12 iterations with 4 subsets. Only point spread function (PSF) modeling (2-mm Gaussian kernel) and attenuation correction were applied. The voxel size was 1 × 1 × 1 mm^3 and the shape matrix size was 217 × 217 × 120.

Engergy and Timing Resolution. Energy and timing resolution were assessed using a scaled-down NEMA scatter fraction phantom with ~10.55 MBq of ^{18}F-FDG. The central axis of the phantom coincided with the PET z-axis, and the radioactive source was positioned based on the TOF-free OSEM reconstructed image. According to the NEMA standard, LORs more than 20 mm from the radioactive source were discarded, and scattering and random events were estimated and subtracted from the tail of the histogram (time bin = 10 ps). We used a six-line source positioned 50 mm from the center to perform system timing calibration. Each line source had an inner diameter of 0.8 mm and a length of 140 mm, with an injected activity of 10.17 MBq for ^{18}F-FDG. Data were acquired for 20 min with an energy window from 461 to 611 keV and the initial coincidence timing window of ± 5 ns.

Langtaosha (LTS) Preprint doi: https://doi.org/10.65215/tr794007 This version posted December 4, 2025. The copyright holder for this preprint (which was not certified by peer review) is the author/funder. Creative Commons license: CC Attribution-NonCommercial-NoDerivatives 4.0 https://creativecommons.org/licenses/by-nc-nd/4.0

Timing calibration was iteratively performed after LOR selection until the change in timing resolution between iterations was less than 1 ps, after which a narrower timing window was applied (11).

C. Phantom Studies

The Multi-layer-Derenzo phantom used in this study was filled with an initial activity of 14.45 MBq of ^{18}F-FDG and scanned for 70 minutes for imaging evaluations. The phantom (Supplemental Figure1) consists of three layers of rod sources with varing diameters: top layer (1.5, 1.6, 1.7, 1.8, 1.9 and 2.0 mm; rod height: 35.5 mm), middle layer (2.0, 2.4, 2.8, 3.2, 3.6 and 4.0 mm; rod height: 20.0 mm) and bottom layer (2.5, 3.0, 3.5, 4.0, 4.5 and 5.0 mm; rod height: 80.0 mm). The rods were arranged in a standard hexagonal pattern, allowing resolution comparisons across a range of feature sizes in a single acquisition. The phantom was positioned at the center of the FOV with a 5-mm offset. Images were reconstructed using the OSEM algorithm (12 iterations, 4 subsets) with PSF modeling (2-mm Gaussian kernel), with and without TOF information. The voxel size was $0.5 \times 0.5 \times 0.5$ mm^3 and the shape matrix size was $217 \times 217 \times 217$. Three experiments were performed; one TOF-enabled central placement is shown in the main text, and the other two (non-TOF, central and 5-cm off-center) are presented in the Supplemental Material.

Additionally, a custom-designed Hoffman brain phantom was prepared and filled with 24.01 MBq of ^{18}F-FDG, followed by 15-minute scan. The phantom had an outer diameter of 210 mm, a thickness of 146 mm, a liquid-filled diameter of 190 mm, and an axial extent of 95 mm. The brain-structure insert consisted of 19 slices, each 5 mm thick, with a maximum diameter of 148.24 mm and the same axial length of 95 mm (Supplemental Figure 2). In this design, the gray matter regions contained radioactivity, whereas the white matter and ventricular regions were non-radioactive. Images were reconstructed using the OSEM algorithm (12 iterations, 4 subsets) with random, attenuation, scatter correction, as well as PSF modeling (3-mm Gaussian kernel) incorporating TOF information. Since the system is not equipped with CT, attenuation correction was performed using a uniform cylindrical attenuation map with the same size as the phantom. The voxel size was $1 \times 1 \times 1$ mm^3 and the shape matrix size was $217 \times 217 \times 120$.

D. Human Study

A 43-y-old male patient with epilepsy participated in a brain ^{18}F-FDG PET protocol approved by the Medical Ethics Committee of the Seventh Affiliated Hospital of Sun Yat-sen University. The blood glucose level was 100.8 mg/dl, and the injected activity was 318.2 MBq.

A comparative evaluation was performed between the SmartBrain PET system and the GE DMI PET/CT scanner. First, an 8-minute PET/CT scan was acquired on the GE DMI at ~60 minutes post-injection, with the subject at rest. Images were reconstructed using OSEM (2 iterations, 17 subsets) with TOF and standard corrections (attenuation, scatter, randoms,

Langtaosha (LTS) Preprint doi: https://doi.org/10.65215/tr794007 This version posted December 4, 2025. The copyright holder for this preprint (which was not certified by peer review) is the author/funder. Creative Commons license: CC Attribution-NonCommercial-NoDerivatives 4.0 https://creativecommons.org/licenses/by-nc-nd/4.0

normalization, calibration, dead time). The voxel size was 1.30208 × 1.30208 × 2.79 mm³ and the shape matrix size was 384 × 384 × 71.

Subsequently, a 60-minute PET scan on the SmartBrain PET system was performed at 190 minutes' post-injection (activity ~95.87 MBq). Images were reconstructed using OSEM (12 iterations, 4 subsets) with random, attenuation, and scatter corrections, as well as PSF modeling (3-mm Gaussian kernel) incorporating TOF information. The reconstructed images contained 217 × 217 × 120 voxels with a voxel size of 1 × 1 × 1 mm³. CT images from the GE DMI PET/CT were used for attenuation correction.

III. Results

A. The results of NEMA NU 2-2018 Performance Evaluation

The averaged FBP2D spatial resolution at the center of the axial FOV was 2.29 mm, as shown in TABLE 1. The apparent Gibbs phenomenon observed at off-center positions is more likely due to limited angular sampling and crystal width. By adding background noise and performing 1000 iterations of the reconstruction algorithm (12), the spatial resolution converged to 1.7 mm (Supplemental Figure 3 and Supplemental Figure 4), which is consistent with the Derenzo phantom results (Supplemental Figure 5). The total system sensitivity was 720.15 cps/MBq at the center in 461-611 keV in Figure 2 (B). The measured average system TOF resolution was 234.22 ps in Figure 2 (C), and the energy resolution was 10.81% (at FWHM). The peak noise-equivalent count rate was 4.67 kcps at an activity concentration of 10.11 kBq/mL in Figure 2 (D), and scatter fraction was 29.53%. The NEMA image-quality contrast recovery coefficients varied from 72.85% (10-mm sphere) to 89.40%, and the background variability (BV) varied was 11.25% (12 iterations and 4 subsets) in TABLE 2.

B. The results of Phantom Studies

Figure 3 shows multi-layer Derenzo phantom at the center of the FOV with TOF-OSEM, where the 1.7-mm hot rods were clearly separated. Supplemental Figure 5 further demonstrates that all 1.7-mm rods exhibited valley-to-peak ratios below 0.735, confirming effective separation. In addition, Supplemental Figure 6 illustrates that even without TOF reconstruction, the 1.7-mm rods remained resolvable both at the central and 5-cm off-center positions, indicating robust spatial resolution across the FOV.

Figure 4 shows reconstructed images of the Hoffman brain phantom. Transaxial, coronal, and sagittal slices demonstrate clear visualization of cortical gray matter activity, with distinct separation from non-radioactive white matter and ventricular regions. The images reproduce the complex gyral patterns of the cortex, highlighting the system's ability to resolve detailed brain anatomy. These findings complement the Derenzo phantom results, confirming both fine spatial resolution and realistic brain-structure imaging capability.

Langtaosha (LTS) Preprint doi: https://doi.org/10.65215/tr794007 This version posted December 4, 2025. The copyright holder for this preprint (which was not certified by peer review) is the author/funder. Creative Commons license: CC Attribution-NonCommercial-NoDerivatives 4.0 https://creativecommons.org/licenses/by-nc-nd/4.0

C. The results of Human Study

Figure 5 shows reconstructed human brain images acquired with the SmartBrain PET system. Transaxial, coronal, and sagittal views clearly depict cortical uptake patterns, with well-defined gray matter distribution and preserved gyral anatomy. The white matter and ventricular regions exhibited low-to-no activity, consistent with the expected ^{18}F-FDG distribution. These images confirm that the SmartBrain system can reliably capture fine structural details of the human brain, even in prolonged acquisitions.

Figure 6 compares brain images acquired with the SmartBrain PET system and the GE DMI PET/CT scanner. The GE DMI PET/CT images (top row) demonstrate high image quality under conventional whole-body PET/CT conditions. The SmartBrain images (bottom row) similarly reveal detailed cortical uptake patterns, with distinct gyral structures. Notably, the SmartBrain PET demonstrated enhanced visualization of cortical features (red arrows) despite the later imaging time point (~190 min post-injection, with reduced activity). This comparison highlights the SmartBrain system's high spatial resolution, supporting its suitability for brain-focused clinical research.

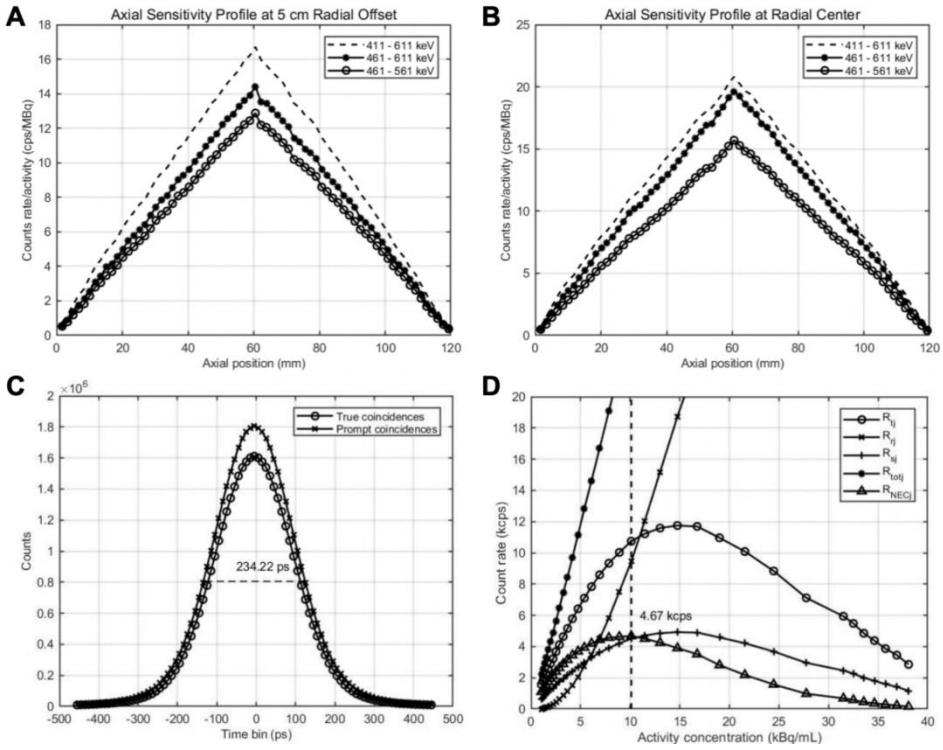

FIGURE 2. (A) Axial sensitivity profile with the line source at 5-cm radial offset. (B) Axial sensitivity profile with the line source at the center of the FOV. (C) TOF resolution with 20 ps time bins. (D) Trues, randoms, scatters, prompts, and noise-equivalent count rate.

Langtaosha (LTS) Preprint doi: https://doi.org/10.65215/tr794007 This version posted December 4, 2025. The copyright holder for this preprint (which was not certified by peer review) is the author/funder. Creative Commons license: CC Attribution-NonCommercial-NoDerivatives 4.0 https://creativecommons.org/licenses/by-nc-nd/4.0

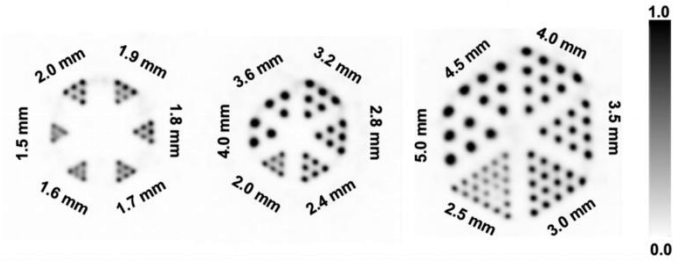

FIGURE 3. Multi-layer-Derenzo phantom imaging. Reconstructed images demonstrate hot-rod groups with diameters ranging from 1.5 to 5.0 mm.

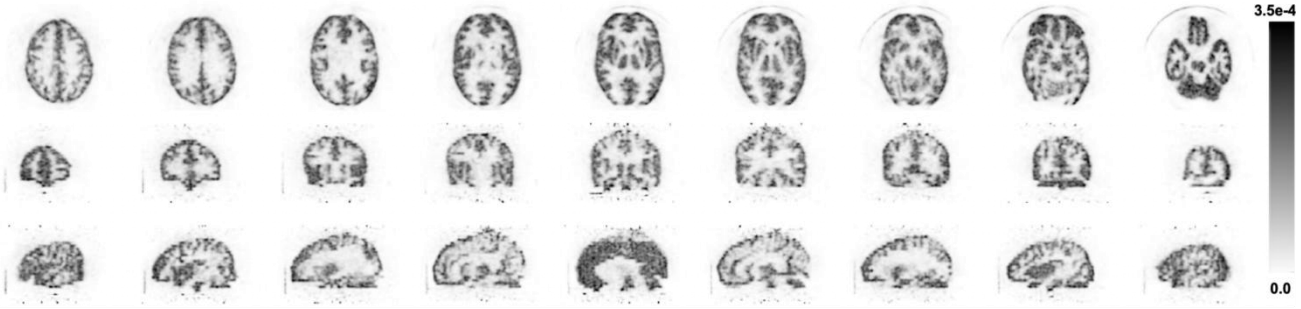

FIGURE 4. Hoffman brain phantom imaging results. Representative transaxial (top row), coronal (middle row), and sagittal (bottom row) slices reconstructed with TOF-OSEM. The gray matter shows distinct uptake, while white matter and ventricular regions exhibit no activity, allowing cortical structures and gyral patterns to be clearly visualized.

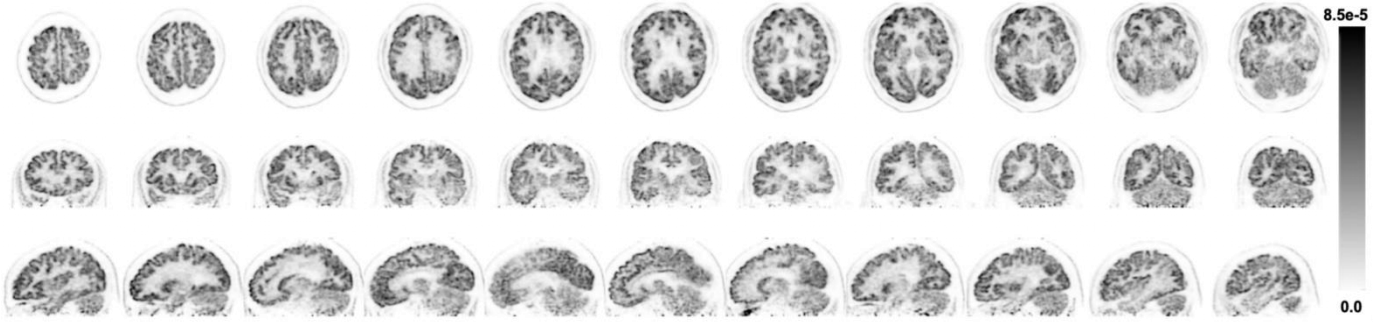

FIGURE 5. Human brain ^{18}F-FDG images acquired with the SmartBrain PET system. Transaxial (top), coronal (middle), and sagittal (bottom) views show clear cortical uptake and preserved gyral structures.

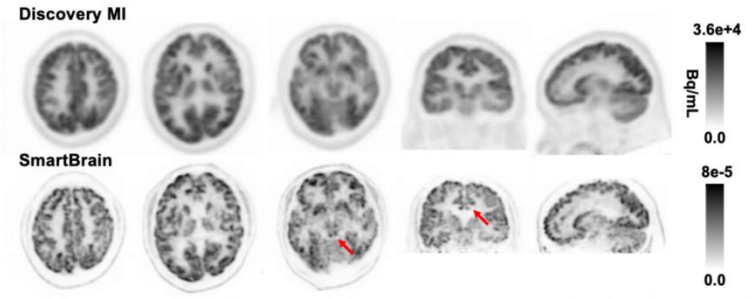

FIGURE 6. Comparison of human brain ^{18}F-FDG images between the GE DMI PET/CT (top row) and the SmartBrain PET system (bottom row). Both systems reveal cortical uptake patterns, while SmartBrain provides enhanced delineation of gyral details (red arrows). DMI images are displayed in calibrated units (Bq/mL). SmartBrain images were not cross-calibrated; the reconstructed voxel values are proportional to activity concentration but expressed in relative units.

Langtaosha (LTS) Preprint doi: https://doi.org/10.65215/tr794007 This version posted December 4, 2025. The copyright holder for this preprint (which was not certified by peer review) is the author/funder. Creative Commons license: CC Attribution-NonCommercial-NoDerivatives 4.0 https://creativecommons.org/licenses/by-nc-nd/4.0

IV. Discussion

The SmartBrain PET system represents one of the few truly wearable brain PET systems capable of imaging under free-moving conditions. It demonstrated excellent spatial resolution, with point-source measurements at the center yielding 2.29 mm and clear resolution of 1.7 mm rods in the multi-layer Derenzo phantom, meeting the requirements for human brain imaging. In human studies, although the sensitivity of the wearable system is lower than the GE DMI PET/CT system (13), a 60-minute scan acquired after low-dose ^{18}F-FDG injection provided clear delineation of brain structures (Figure 5), with good comfort and feasibility during wear. Furthermore, after applying delay calibration algorithms, the system achieved a timing resolution of 234.22 ps. These results highlight the potential for future human imaging with higher tolerated activity and reduced scan times.

Several design features contribute to SmartBrain's performance. First, its full-ring configuration ensures complete FOV coverage with spatial resolution maintained across both central and off-center regions. Second, the use of short 5-mm crystals minimizes DOI uncertainty and reduces Compton scatter within the crystal. Third, the 3-mm crystal pitch further limits inter-crystal scatter and supports high-resolution imaging. Fourth, the compact bore size (20 cm) decreases the impact of non-collinearity, which is particularly advantageous in brain imaging. Finally, the incorporation of TOF (14, 15) reconstruction significantly improves image quality and compensates for reduced sensitivity relative to large clinical PET/CT systems. Together, these elements explain why SmartBrain achieves high spatial resolution and clear visualization of brain structures despite its compact and lightweight design.

Compared to conventional brain PET systems (16, 17), SmartBrain offers unique advantages in mobility, cost, and user comfort. Systems (18, 19) such as Vrain (20) and NeuroExplorer (21) achieve high sensitivity and image quality but remain large and stationary. In contrast, SmartBrain's compact detector design, lightweight electronics, and optimized mechanical structure significantly reduce system weight and cost, enabling wearable use. Compared with previous wearable PET prototypes such as AM-PET (22) and MindTracker, SmartBrain shows improvements in spatial resolution and axial coverage, and supports dynamic imaging under naturalistic conditions. Design elements such as flexible padding and ergonomic support help minimize motion-related artifacts during wear.

Nonetheless, current limitations remain. The system's thinner crystals result in lower sensitivity, and while TOF has been implemented, further improvements in detector coverage and sensitivity are needed. In addition, the absence of pile-up correction constrains performance under higher count-rate conditions, and fast dynamic studies remain challenging. Future optimization—including enhanced detector geometry, advanced correction algorithms, and AI-assisted image reconstruction (23,

Langtaosha (LTS) Preprint doi: https://doi.org/10.65215/tr794007 This version posted December 4, 2025. The copyright holder for this preprint (which was not certified by peer review) is the author/funder. Creative Commons license: CC Attribution-NonCommercial-NoDerivatives 4.0 https://creativecommons.org/licenses/by-nc-nd/4.0

24, 25) will further improve image quality, reduce acquisition times, and expand the scope of clinical and neuroscientific applications.

V. Conclusion

In this study, we developed and validated the SmartBrain wearable brain PET system, which demonstrated human-level spatial resolution and dynamic imaging capabilities under free-moving conditions. The system's lightweight, compact design and wearable configuration offer new opportunities for brain PET imaging beyond the constraints of conventional static systems. The system now incorporates TOF reconstruction (timing resolution ~234 ps) and an optimized pile-up handling pipeline; remaining limitations are primarily lower sensitivity relative to whole-body PET/CT due to thinner crystals and limited detector coverage. Ongoing hardware (e.g., extended axial coverage) and software refinements (enhanced attenuation modeling and advanced/AI-assisted reconstruction) are expected to further improve image quality and quantitative accuracy. With continued improvements, SmartBrain has strong potential to support advanced neuroscience research and expand clinical applications in neurodegenerative diseases, movement disorders, and cognitive studies in naturalistic environments.

Disclosure

This work was supported by the National Natural Science Foundation of China (Grant no. 82327809), National Key Research and Development Program of China (Grant No. 2024YFF0727400, 2024YFF0507700). This work was supported by Shenzhen Bay Laboratory High Performance Computing and Informatics Core. No potential conflicts of interest relevant to this article was reported. This study was approved by the Medical Ethics Committee of the Seventh Affiliated Hospital of Sun Yat-sen University (Approval No. KY-2024-354-02). All patients provided written informed consent prior to participation.

Key points

QUESTION: What is the performance of the SmartBrain PET, according to the NEMA NU 2-2018 standard?

PERTINENT FINDINGS: The SmartBrain PET provides a spatial resolution below 1.7 mm, a sensitivity of 720.15 cps/MBq, and a timing resolution of 234.22 ps.

IMPLICATIONS FOR PATIENT CARE: The SmartBrain PET system enables ambulatory imaging with enhanced cost-efficiency and a space-saving design, positioning it as a scalable solution for precision diagnostics in both clinical and community healthcare settings.

Langtaosha (LTS) Preprint doi: https://doi.org/10.65215/tr794007 This version posted December 4, 2025. The copyright holder for this preprint (which was not certified by peer review) is the author/funder. Creative Commons license: CC Attribution-NonCommercial-NoDerivatives 4.0 https://creativecommons.org/licenses/by-nc-nd/4.0

REFERENCES

1. Miyazaki T, Nakajima W, Hatano M et al. Visualization of AMPA receptors in living human brain with positron emission tomography. Nat Med. 2020;26:281–288.

2. Van Dyck CH, Swanson CJ, Aisen P, et al. Lecanemab in early Alzheimer's disease. N Engl J Med. 2023;388:9–21.

3. Yamamoto S, Honda M, Oohashi T, et al. Development of a brain PET system, PET-Hat: a wearable PET system for brain research. IEEE Trans Nucl Sci. 2011;58:668–673.

4. Tashima H, Yoshida E, Nishikido F, et al. Development of the helmet-chin PET prototype. IEEE Nucl Sci Symp Med Imaging Conf (NSS/MIC). 2015:1–3.

5. Melroy S, Bauer C, McHugh M, et al. Development and design of next-generation head-mounted ambulatory microdose positron-emission tomography (AM-PET) system. Sensors (Basel). 2017;17:1164.

6. Xu J, Zhao Z, Xie S, et al. Mind-tracker PET: a wearable PET camera for brain imaging. IEEE Nucl Sci Symp Med Imaging Conf (NSS/MIC). 2017:1–2.

7. Majewski S. The path to the "ideal" brain PET imager: the race is on, the role for TOF PET. Nuovo Cimento C. 2020;43:1–35.

8. Yu X, Liu H, Zhao H, et al. A multiplexing method based on multidimensional readout method. Phys Med Biol. 2025;70(4)

9. Tao W, Weng F, Chen G, et al. Design study of fully wearable high-performance brain PETs for neuroimaging in free movement. Phys Med Biol. 2020;65:135006.

10. National Electrical Manufacturers Association. NEMA Standards Publication NU 2-2018: performance measurements of positron emission tomographs. Rosslyn, VA: Natl Electr Manuf Assoc; 2018.

11. Zeng T, Yang H, Cao T, et al. Timing calibration comparison research of integrated TOF PET/MR. Sheng Wu Yi Xue Gong Cheng Xue Za Zhi. 2019;36:1003–1011.

12. Gong K, Cherry SR, Qi J. On the assessment of spatial resolution of PET systems with iterative image reconstruction. Phys Med Biol. 2020;65:225001

13. Pan T, Einstein SA, Kappadath SC, et al. Performance evaluation of the 5‐Ring GE Discovery MI PET/CT system using the National Electrical Manufacturers Association NU 2‐2012 Standard. Med Phys. 2019;46:3025–3033.

14. Surti S, Karp JS. Update on latest advances in time-of-flight PET. Phys Med. 2020;80:251–258.

15. Gonzalez-Montoro, A., Pavón, N., Barberá, J. et al. Design and proof of concept of a double-panel TOF-PET system. EJNMMI Phys 11, 73 (2024).

Langtaosha (LTS) Preprint doi: https://doi.org/10.65215/tr794007 This version posted December 4, 2025. The copyright holder for this preprint (which was not certified by peer review) is the author/funder. Creative Commons license: CC Attribution-NonCommercial-NoDerivatives 4.0 https://creativecommons.org/licenses/by-nc-nd/4.0

16. Catana C. Development of dedicated brain PET imaging devices: recent advances and future perspectives. J Nucl Med. 2019;60:1044–1052.

17. Moliner L, Rodríguez-Alvarez MJ, Catret JV, et al. NEMA performance evaluation of CareMiBrain dedicated brain PET and comparison with the whole-body and dedicated brain PET systems. Sci Rep. 2019;9:15484.

18. Bartlett EA, Lesanpezeshki M, Anishchenko S, et al. Dynamic Human Brain Imaging with a Portable PET Camera: Comparison to a Standard Scanner. J Nucl Med. 2024;65(2):320-326.

19. Zhou F, D'Ascenzo N, Zhang B, et al. Development and evaluation of a portable MVT-based all-digital helmet PET scanner. IEEE Trans Radiat Plasma Med Sci. 2024;8:287–294.

20. Akamatsu G, Takahashi M, Tashima H, et al. Performance evaluation of VRAIN: a brain-dedicated PET with a hemispherical detector arrangement. Phys Med Biol. 2022;67:225011.

21. Li H, Badawi RD, Cherry SR, et al. Performance characteristics of the NeuroEXPLORER, a next-generation human brain PET/CT imager. J Nucl Med. 2024;65:1320–1326.

22. Siva NK, Bauer C, Glover C, et al. Real-time motion-enabling positron emission tomography of the brain of upright ambulatory humans. Commun Med. 2024;4:117.

23. Hu R, Li C, Tian K, Cui J, Chen Y, Liu H. Deep unrolled primal dual network for TOF-PET list-mode image reconstruction. Phys Med Biol. 2025;70(17).

24. Schramm G, Holler M. Fast and memory-efficient reconstruction of sparse Poisson data in listmode with non-smooth priors with application to time-of-flight PET. Phys Med Biol. 2022;67(15).

25. Murat H, Zulkifli MAA, Said MA, Awang Kechik M, Tahir D, Abdul Karim MK. Optimizing time-of-flight of PET/CT image quality via penalty β value in Bayesian penalized likelihood reconstruction algorithm. Radiography (Lond). 2025;31(1):343-349.

Langtaosha (LTS) Preprint doi: https://doi.org/10.65215/tr794007 This version posted December 4, 2025. The copyright holder for this preprint (which was not certified by peer review) is the author/funder. Creative Commons license: CC Attribution-NonCommercial-NoDerivatives 4.0 https://creativecommons.org/licenses/by-nc-nd/4.0

TABLE 1. INTRINSIC SPATIAL RESOLUTION MEASUREMENT

No	Z	X Offset (cm)	Average	Radial	Tangential	Axial
1	1/2	0	2.29	2.50	2.77	1.61
2		1	2.49	2.84	3.02	1.61
3		2	2.44	2.58	3.12	1.61
4		3	2.72	2.83	3.71	1.61
5		4	2.65	2.06	4.27	1.61
6		5	2.93	2.74	4.46	1.61
7		6	3.41	2.34	6.29	1.61
8		7	3.52	1.95	7.00	1.61
9	1/8	0	2.87	3.25	2.27	3.08
10		1	3.24	3.53	3.13	3.06
11		2	3.04	2.89	3.16	3.06
12		3	3.09	3.01	3.20	3.05
13		4	3.21	3.00	3.61	3.03
14		5	3.18	2.93	3.60	3.01
15		6	3.44	2.83	4.52	2.97
16		7	3.48	2.70	4.69	3.05

TABLE 2. CONTRAST RECOVERY COEFFICIENT AND BACKGROUND VARIABILITY FOR 12 ITERATIONS WITH 4 SUBSETS OF OSEM RECONSTRUCTION

Items	Sphere diameter j mm	Value
QH,j	10 mm	72.85%
	13 mm	76.88%
	17 mm	81.73%
	22 mm	80.40%
	28 mm	80.26%
	37 mm	89.40%
Nj	10 mm	11.25%